

Probing Porosity and Pore Interconnectivity in Self-Assembled TiO₂–Graphene Hybrid Nanostructures Using Hyperpolarized ¹²⁹Xe NMR

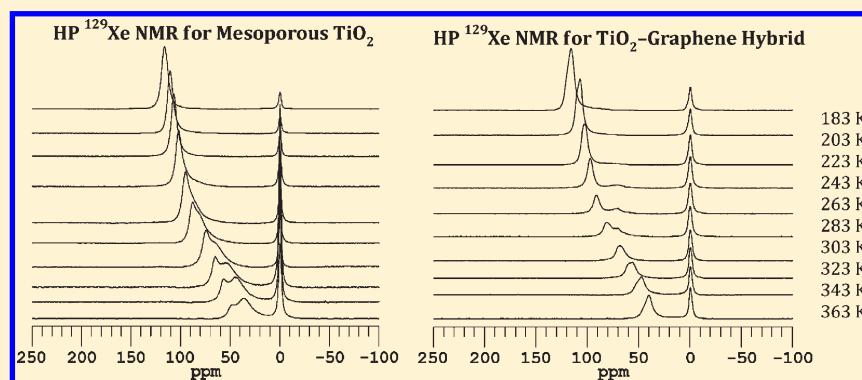
Li-Qiong Wang,^{*,†} Donghai Wang,[‡] Jun Liu,[§] and Gregory J. Exarhos[§]

[†]Department of Chemistry, Brown University, Providence, Rhode Island 02912, United States

[‡]Department of Mechanical Engineering, Pennsylvania State University, University Park, Pennsylvania 16802, United States

[§]Fundamental & Computational Sciences Directorate, Pacific Northwest National Laboratory, Richland, Washington 99354, United States

ABSTRACT:



Hyperpolarized (HP) ¹²⁹Xe NMR was used to probe the porosity and interconnectivity of pores in self-assembled hybrid TiO₂–graphene nanostructures. We have demonstrated that HP ¹²⁹Xe NMR is a powerful technique in probing any changes in porosity and interconnectivity of the pores caused by the addition of a small amount of functionalized graphene sheets (FGSs) (1% weight percent) into the network of mesoporous TiO₂. To obtain the information on the changes in porosity and interconnectivity of the pores caused by the addition of a small amount of FGSs, a comparative study has been carried out by acquiring HP ¹²⁹Xe NMR spectra under identical experimental conditions for both pure mesoporous TiO₂ and hybrid TiO₂–FGSs. The HP ¹²⁹Xe NMR results from our comparative study suggest that TiO₂ and graphene are mixed uniformly on the nanoscale and the resulting hybrid nanostructure has better channel connectivity between different domains, enhancing the transport property for Li-insertion/extraction.

INTRODUCTION

There has been increased interest in developing hybrid nanostructured materials with controlled porosity for electrochemical energy storage and other energy related applications. The extent of interconnectivity between nano- or mesopore domains in such materials markedly affects their transport properties. Therefore, characterization of resident porosity and pore interconnectivity is key to better understanding ion transport mechanisms in nanoporous materials.

The pore geometry in most porous materials, even in ordered mesoporous silica, is complex and is exemplified by interconnected cages, channels, and micropores.¹ As a result of these complex topologies and buried interfacial structures, characterization of pore interconnectivity in nano- or mesoporous materials is often challenging and mandates application of several characterization methods. The most common techniques such as small-angle X-ray or neutron scattering, and gas absorption,

however, do not provide direct information on how channels and cages are connected.

Over the years, ¹²⁹Xe NMR has developed into a powerful and robust method for probing the void structure in extremely high surface area porous solids.^{2–5} The large chemical shift range of ¹²⁹Xe is strongly dependent on both local environmental and chemical factors such as the composition of the matrix, nature and concentration of coadsorbed molecules, and the shape and size of inherent void spaces.^{2–5} The use of optical pumping approaches for the production of hyperpolarized (HP) xenon permits a dramatic increase in the sensitivity of ¹²⁹Xe NMR up to a factor of 10⁴,⁶ thereby enabling these pore characterization studies. Using HP xenon produced under continuous flow (CF)

Received: May 20, 2011

Revised: December 9, 2011

Published: December 09, 2011

conditions, measurements are possible at very low xenon concentration, which minimizes the contribution from Xe–Xe interactions to the observed chemical shift. As such, the observed ^{129}Xe chemical shifts can be assigned principally to interactions between the xenon atoms and the porous surfaces. Because spin-polarized Xe gas percolates through the interconnected pores and samples the local pore environments, HP ^{129}Xe NMR has the unique advantage of directly probing not only these buried interfaces but also the interconnectivity between the pores.

TiO_2 has been extensively studied to understand correlations between nanostructure and charge migration through the structure.^{7–15} TiO_2 is studied because it is an abundant, low cost, and environmentally benign material. It is also structurally stable during Li insertion/extraction and is intrinsically safe through retardation of electrochemical deposition of lithium. These properties make TiO_2 particularly attractive for large-scale energy storage. An approach to improve Li-ion insertion properties invokes substitution of hybrid nanostructured electrodes that combine nanostructured electrode materials with other conductive additive nanophases. To improve high-rate charge/discharge performance and reduce the cost of electrochemically active materials, it is important to identify high surface area, inexpensive, and highly conductive nanostructured materials that can be integrated with electrochemically active materials at the nanoscale.

Our study is focused on understanding pore structure in a ceramic hybrid material derived from a surfactant-directed processing approach that produces highly crystalline and stable mesoporous TiO_2 with a surface area approaching $300\text{ m}^2/\text{g}$ and containing tunable pore sizes from 2 to 4 nm.¹⁶ Unlike the more traditional mesoporous TiO_2 materials having semicrystalline or nanocrystalline walls,^{17–24} the new materials are comprised of extended, locally aligned nanorod-like building blocks. The porosity and interconnectivity of these nanopore channels have been examined using HP ^{129}Xe NMR.²⁵ Pores of 4 nm size resident in mixed anatase and rutile mesoporous TiO_2 phases were identified. Complementary to other pore characterization techniques, HP ^{129}Xe NMR is able to probe the interconnectivity between pores present in these different phases. The substantial pore interconnectivity in TiO_2 is associated with an enhanced Li ion insertion rate.

To further increase the Li ion insertion rate and capacity, a nanostructured TiO_2 –graphene hybrid material has been prepared by means of an anionic surfactant mediated self-assembly growth process described in our recent paper.²⁶ Graphene is a two-dimensional macromolecular sheet of carbon atoms with a honeycomb structure that exhibits excellent electronic conductivity and mechanical stability.^{27–30} Hybrid materials synthesized here showed significantly enhanced Li-ion insertion/extraction in TiO_2 . The specific capacity more than doubled at high charge rate, as compared to the pure TiO_2 phase, indicating that incorporation of these conducting graphene sheets has the potential to markedly improve the performance of Li ion battery electrode materials.

In this Article, variable-temperature HP ^{129}Xe NMR spectroscopy is applied to probe the porosity and interconnectivity of self-assembled TiO_2 –FGSs (functionalized graphene sheets) hybrids. Results obtained for hybrid TiO_2 –FGSs are compared to those for single phase mesoporous TiO_2 . Our HP ^{129}Xe NMR study addresses several important issues including FGSs insertion into the network of mesoporous TiO_2 , uniformity of TiO_2 /FGSs mixtures at the nanoscale, and fluctuations in porosity and interconnectivity of pores in TiO_2 nanostructures caused by

addition of FGSs into the mesoporous TiO_2 network. Such information is critical for understanding the role of graphene in Li ion insertion/extraction kinetics.

■ EXPERIMENTAL SECTION

Materials Synthesis and Characterization. Three types of materials were used in HP ^{129}Xe NMR measurements. XRD, TEM, and XPS were used for characterizing these materials. XRD patterns were obtained on a Philips Xpert X-ray diffractometer using Cu $K\alpha$ radiation at $\lambda = 1.54\text{ \AA}$. The TEM imaging was performed on a JEOL JSM-2010 TEM operated at 200 kV. XPS characterization was performed using a Physical Electronics Quantum 2000 scanning ESCA microprobe with a focused monochromatic Al $K\alpha$ X-ray (1486.7 eV) source and a spherical section analyzer.

Functionalized graphene sheets (FGSs) used in this study were prepared by means of thermal expansion of graphite oxide.^{31,32} In comparison to the graphene produced by the chemical reduction of graphene oxide,^{33,34} graphene prepared by the thermal expansion approach can have tunable C/O ratios ranging from 10 to 500, and thus its ionic conductivity can be tuned to higher values. FGSs processing begins with chemical oxidation of graphite flakes to increase the *c*-axis spacing from 0.34 to 0.7 nm as described elsewhere.^{33,34} The resultant graphite oxide is then split by a rapid thermal expansion to yield separated graphene sheets. X-ray photoemission spectroscopy (XPS) of FGSs shows a single sharp C1s peak at a binding energy of 284.6 eV, indicating a high degree of sp^2 conjugation. A small shoulder at 286 eV indicates the existence of some C–O bonds corresponding to the epoxy and hydroxyl functional groups on the FGSs.

Mesoporous crystalline TiO_2 was prepared according to a previous report¹⁶ using a one-step low-temperature crystallization approach. In a typical synthesis, 1.2 mL of 0.5 M sodium dodecyl sulfate ($\text{C}_{12}\text{H}_{25}\text{SO}_4\text{Na}$) (SDS) solution (0.6 mmol) was added into 10 mL of 0.12 M TiCl_3 solution (1.2 mmol) under vigorous stirring. Subsequently, 0.8 mL of 1.0 wt % H_2O_2 solution (0.26 mmol) was added dropwise under vigorous stirring. The mixture was then diluted to a total volume of 55 mL by adding deionized water and further stirred in a polypropylene flask at $60\text{ }^\circ\text{C}$ for 15 h. The precipitates were separated by centrifuge followed by washing with deionized water and ethanol. Next, the product was dried in a vacuum oven at $60\text{ }^\circ\text{C}$ overnight and subsequently calcined in static air at $400\text{ }^\circ\text{C}$ for 2 h.

The functionalized hybrid TiO_2 –FGSs were also prepared using a one-step low temperature self-assembly route similar to that for the synthesis of mesoporous TiO_2 .²⁶ A mild, low-temperature (below $100\text{ }^\circ\text{C}$) crystallization process was carried out to form crystalline TiO_2 having a controlled crystalline phase (i.e., rutile or anatase) on the graphene sheets.^{26,35} The low temperature condition was also important in preventing aggregation of graphene sheets at elevated temperatures.³⁶ In line with our previous studies using a low-temperature oxidative hydrolysis and crystallization process, rutile-phase TiO_2 –FGSs is obtained containing a minor anatase phase.

In a typical preparation of rutile TiO_2 –FGSs hybrid materials (e.g., 1 wt % FGSs), 4.8 mg of FGSs and 3 mL of SDS aqueous solution (0.5 mol/L) were mixed together. The mixture was diluted to 15 mL and sonicated for 10–15 min (Branson Sonifer S-450A, 400 W). A 25 mL portion of TiCl_3 (0.12 mol/L)

aqueous solution was added to as-prepared SDS–FGS dispersions while stirring. Next, 2.5 mL of H_2O_2 (1 wt %) was added dropwise followed by deionized water under vigorous stirring until a total volume of 80 mL was achieved. All resulting mixtures were further stirred in a sealed polypropylene flask at 90 °C for 16 h. The precipitates were separated by centrifugation followed by washing with deionized water and ethanol. The centrifuging and washing processes were repeated three times. The product was then dried in a vacuum oven at 70 °C overnight and subsequently calcined in ambient air at 400 °C for 2 h. The thermal gravimetric analysis (TGA) indicated an approximate 50 wt % loss of FGSs following calcination in air at 400 °C for 2 h.

HP ^{129}Xe NMR Measurements. HP ^{129}Xe NMR experiments were carried out on a Chemagnetics spectrometer operating at 82.98 MHz (magnetic field 7.05 T) using a specially designed variable-temperature double-resonance magic angle spinning (MAS) probe with a continuous flow (CF) of HP xenon. For ^{129}Xe NMR experiments, a single-pulse (SP) Bloch-decay method was used, and samples were loaded into 7.5 mm Zirconia PENCIL rotors. The ^{129}Xe NMR experiments were performed with non spinning. SP spectra were collected with a 4.5 μs (90°) ^{129}Xe pulse and a repetition delay of 1 s. The number of transients was 100.

In collaboration with Prof. Brian Saam's group at university of Utah, we have recently designed and constructed a highly efficient HP Xe ^{129}Xe polarizer that provided probe nuclei for this investigation. This Xe polarizer has a unique design and is based upon a report by the Hersman group.³⁷ Unlike most of the HP xenon polarizers available in other laboratories, a low-pressure environment is used in this design to mitigate quenching efficient transfer of spin from the excited Rb electron manifold to the Xe nucleus. Effective use of the pump diode laser power (80 W) at 795 nm is provided by means of a long path-length cell (1 m), high Rb vapor density, and by counter flowing the spin exchanged optically pumped (SEOP) gas in a direction opposite to that of the laser propagation direction. This unique arrangement achieves a remarkably high polarization rate (>35%), even at high flow velocity. With this enhanced sensitivity, our new ^{129}Xe NMR polarizer will enable future studies of materials having relatively low surface area such as thin porous membranes and self-assembled structures in solution.

A xenon–helium–nitrogen mixture with a volume composition of 1%–66%–33% was used in all CF HP experiments. The flow rate was kept constant in the range of about 500 scc/min (gas flow normalized to standard conditions). In CF HP experiments, the HP xenon flow was delivered directly from the polarizer to the coil region of the NMR probe through 1.5 mm ID plastic tubing. Variable-temperature NMR experiments in the 183–333 K range were performed using a PNNL-designed cell and temperature controller. The temperature inside the NMR coil of the CF probe was calibrated using the ^{207}Pb resonance in $\text{Pb}(\text{NO}_3)_2$.³⁸ All measured ^{129}Xe NMR chemical shift data were referenced to the xenon gas chemical shift extrapolated to zero pressure (0 ppm).

RESULTS AND DISCUSSION

Detailed characterization of pure mesoporous TiO_2 and hybrid TiO_2 –FGSs appears in earlier published papers.^{16,26} Their characteristic physical properties including crystalline phase, nanostructure, surface area, and pore size are summarized below. For pure mesoporous TiO_2 , the low-angle X-ray diffraction pattern of mesoporous TiO_2 displays a reflection peak at a

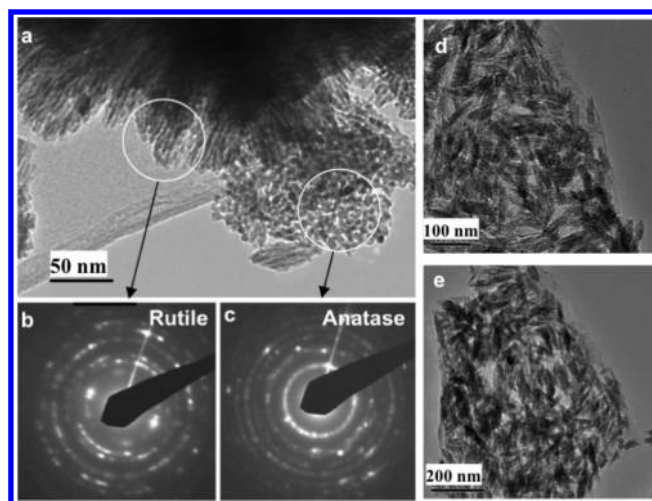


Figure 1. (a) TEM image of aggregated spherical anatase particles residing outside of the nanorod-based mesoporous rutile region for pure mesoporous TiO_2 . (b) SAED pattern from the oriented nanorod-based mesoporous rutile for pure mesoporous TiO_2 . (c) SAED pattern from the spherical nanoparticle-based mesoporous anatase for pure mesoporous TiO_2 . (d and e) High- and low-magnification TEM images of the self-assembled rutile TiO_2 –FGS hybrids, respectively.

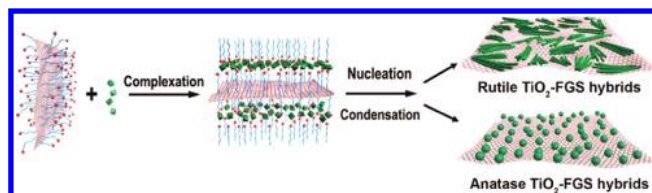


Figure 2. Schematic drawing of the anionic sulfate surfactant-mediated stabilization of graphene and growth of self-assembled TiO_2 –FGS hybrid nanostructures. The green rods represent the rutile phase nanorods, while the planar purple mesh corresponds to the individual graphene sheet.

d -spacing of 7.4 nm, indicative of short-range mesoscale ordering. High angle XRD patterns confirm that as-synthesized materials contain crystalline rutile TiO_2 with a small amount of anatase TiO_2 . Results from nitrogen sorption measurements show type-IV isotherms with a rather narrow size distribution of mesopores. The adsorption data indicate a Brunauer–Emmett–Teller (BET) surface area of 300 m^2/g for mesoporous TiO_2 after calcination. The average pore size in the calcined mesoporous TiO_2 calculated using the Barrett–Joyner–Halenda (BJH) model is 3.1 nm. From our previous studies,^{16,26} XRD for both pure mesoporous TiO_2 and TiO_2 –FGSs show almost identical patterns (ref 16, Figure 1b and ref 26, Figure 2) containing a majority of rutile TiO_2 with the same amount of minor anatase TiO_2 of nearly 5% (the detailed quantification of the anatase phase is given in ref 16).

Transmission electron microscopy (TEM) images for both pure mesoporous TiO_2 and TiO_2 –FGSs are displayed in Figure 1. For pure mesoporous TiO_2 , rodlike rutile nanocrystals are oriented in parallel and interspaced by mesoporous channels (Figure 1a). Aggregates of spherical anatase nanoparticles that reside outside of the nanorod-based mesoporous rutile also are observed. Selected area electron diffraction (SAED) patterns (Figure 1b and c) further confirm the rutile crystalline phase for

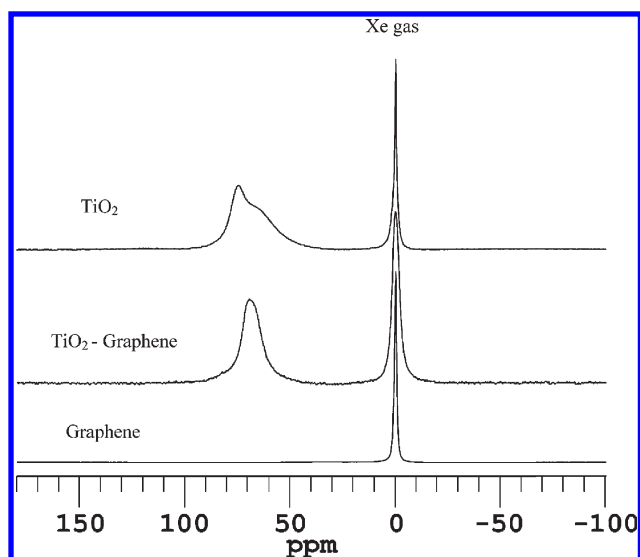


Figure 3. HP ^{129}Xe NMR spectra taken at 298 K before heating for TiO_2 -FGS hybrid material, pure mesoporous TiO_2 , and pure bulk FGS, respectively.

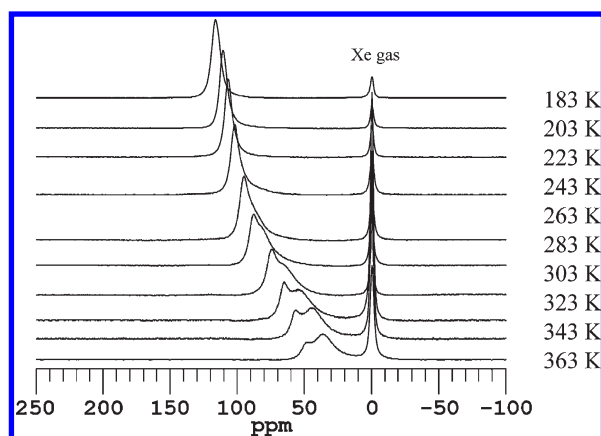


Figure 4. Variable-temperature continuous flow HP ^{129}Xe spectra for pure mesoporous TiO_2 . The top spectrum was recorded at 183 K, and the temperature was raised 20 K for each incremental spectrum up to 363 K.

the oriented rodlike nanocrystals and the anatase phase for the spherical nanoparticle aggregates. In agreement with the high angle XRD patterns, a series of high-resolution TEM images shows that the oriented rutile TiO_2 nanorods comprise the dominant structures in mesoporous TiO_2 in addition to a much lower quantity of spherical anatase nanoparticles. TEM images for hybrid- TiO_2 graphene are given in Figure 1d and e where the FGSs are covered with rodlike rutile nanocrystals similar to those seen for pure mesoporous TiO_2 . Both the edge of the graphene sheet and the nanostructure of TiO_2 are seen clearly in the high-magnification image of Figure 1d. The nanostructured TiO_2 is comprised of parallel rodlike rutile nanocrystals interspaced with the SDS surfactant. This structure is consistent with that observed in our previous studies detailing the formation of mesoporous rutile.¹⁶ On the basis of the high-resolution TEM and XRD data, a schematic drawing for the formation of self-assembled rutile (major phase) and anatase (minor phase) TiO_2 -FGS hybrid nanostructures is presented in Figure 2 where

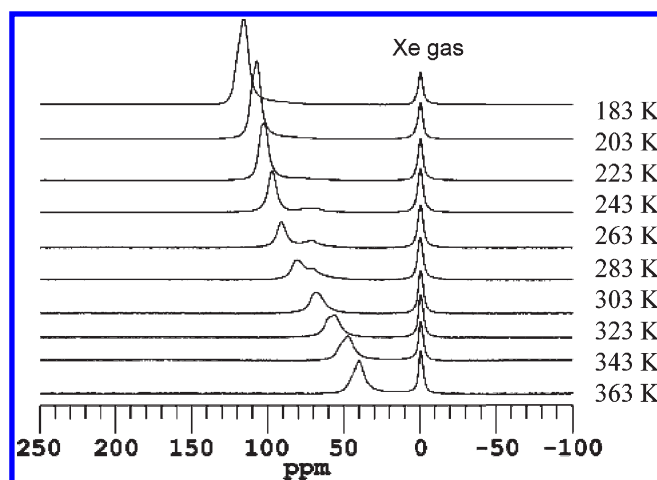


Figure 5. Variable-temperature continuous flow HP ^{129}Xe spectra for self-assembled TiO_2 -FGS hybrids. The bottom spectrum was recorded at 183 K, and the temperature was raised 20 K for each incremental spectrum up to 363 K.

green rods represent rutile nanocrystals while the planar purple mesh corresponds to an individual graphene sheet.

A comparative study of both pure mesoporous TiO_2 and hybrid TiO_2 -FGSs has been carried out to examine any subtle changes in the porosity and interconnectivity caused by the addition of a small amount of graphene into the networks of mesoporous TiO_2 materials. A series of HP ^{129}Xe NMR spectra were taken under nearly identical conditions for both pure mesoporous TiO_2 and hybrid TiO_2 -FGSs. Figure 3 displays the HP ^{129}Xe NMR spectra taken at 303 K for pure mesoporous TiO_2 , self-assembled rutile TiO_2 -FGS hybrids, and pure bulk functionalized graphene sheets (FGSs), respectively. Each of the three samples was heated to 403 K in a NMR rotor under N_2 flow for 10 min and then slowly cooled to 303 K before taking the spectrum shown in Figure 3. Variable-temperature continuous flow HP ^{129}Xe spectra are given in Figures 4 and 5 for pure mesoporous TiO_2 and self-assembled rutile TiO_2 -FGS hybrids, respectively. The top spectra in Figures 4 and 5 were recorded at 183 K (samples were heat-treated to 403 K for 10 min and then cooled to 173 K for 10 min before taking spectra at 183 K), and the temperature was raised 20 K for each incremental spectrum up to 363 K.

The contrasting spectral features shown in Figure 3 for all three samples are indicative of different pore environments associated with each of these three samples. A sharp resonance peak at 0 ppm is observed in the spectra of all three samples. The 0 ppm peak is associated with the free Xe gas, and the peaks at larger chemical shift correspond to xenon adsorbed within the structure of the material. For pure mesoporous TiO_2 , we observed two resonance peaks at higher chemical shift. In Figure 3, a broader resonance peak with a larger area is found at 63.7 ppm, whereas a comparatively sharper peak but with a smaller peak area is observed at 73.9 ppm. Similar two resonance peaks were also observed in the variable-temperature spectrum (Figure 4) taken at 303 K for pure mesoporous TiO_2 . Furthermore, all spectra taken at $T > 283$ K in Figure 4 consistently show two resonance peaks at higher chemical shift for the pure mesoporous TiO_2 , in agreement with the results from our previous study of pure mesoporous TiO_2 using a different instrument.²⁵ The coexistence of two distinct peaks suggests

that there are at least two different pore environments in pure mesoporous TiO_2 in which Xe can adsorb. Our new HP ^{129}Xe polarizer provides consistent results when compared to a conventional setup used in the previous study.²⁵

In contrast, the HP ^{129}Xe NMR spectrum in Figure 3 taken for hybrid rutile TiO_2 –FGSs displays a single relatively narrow peak at 68.7 ppm. A similar peak is also observed in the spectrum taken at 303 K in Figure 5 for hybrid rutile TiO_2 –FGSs. On the basis of our previous study,²⁵ the two resonance peaks for pure mesoporous TiO_2 are attributed to pores associated with anatase (at higher chemical shift) and rutile TiO_2 , respectively. It is interesting to observe substantial spectral changes in HP ^{129}Xe NMR spectra for mesoporous TiO_2 before and after adding a small amount of FGSs. Several factors including pore structure, interconnectivity of the pores, resident surface chemistry, and composition affect the line shape of the ^{129}Xe NMR resonances. To confirm that functionalized graphene sheets by themselves do not add a new spectral feature to the resonances associated with mesoporous TiO_2 , we also carried out experiments on these bulk FGSs under the same conditions at 303 K after sample is heated to 403 K for 10 min. The spectrum for pure bulk FGSs in Figure 3 does not show any peaks at higher chemical shifts (>50 ppm), suggesting that the FGSs by themselves do not add new ^{129}Xe NMR spectral features to the resonances assigned to the Xe interaction with mesoporous TiO_2 . Because our XRD and TEM data have shown that both hybrid TiO_2 –FGSs and pure mesoporous TiO_2 are comprised of similar rutile nanorods with the same amount of minor anatase TiO_2 , the pore structures, the surface chemical structures, and the composition should be similar in both samples. It is surprising, then, to observe such significant changes in the line shape of the HP ^{129}Xe NMR spectrum for hybrid TiO_2 –FGSs upon adding a very small amount of functionalized graphene.

On the basis of the fact that pure bulk FGSs do not contribute to the HP ^{129}Xe NMR signal to the resonances associated with the mesoporous TiO_2 and that the surface chemistry and composition are identical for pure mesoporous TiO_2 and hydride TiO_2 –FGSs, we conclude that the changes in HP ^{129}Xe NMR line shapes associated with the mesopores in TiO_2 do not result from these factors. In addition, we exclude other factors such as temperature and Xe pressure that could change the ^{129}Xe NMR spectrum by performing the experiments under the same conditions in terms of temperature and ^{129}Xe pressure for both samples. Therefore, the interconnectivity of the pores is most likely the main factor that affects the line shape of the ^{129}Xe NMR resonance for the hydride TiO_2 –FGSs. However, it is difficult to imagine that the addition of a small amount of graphene could make such a large change in the interconnectivity of the pores. To induce such changes, the graphene sheets would have to be well separated and spread out uniformly into the network of the mesoporous TiO_2 . Hence, there is no phase separation between graphene and TiO_2 , in agreement with the TEM data showing that most TiO_2 nanorods are spread out on mostly individual graphene sheets.²⁶ FGSs have extremely high surface area (theoretical value of $2630\text{ m}^2/\text{g}$) especially when produced as chemically functionalized graphene sheets through the thermal expansion of graphite oxide.^{39,40} It is possible that a small addition of graphene sheet to the rutile TiO_2 will impart a significant change to the nanostructure of TiO_2 . Our Xe NMR data confirm that the graphene sheets are well mixed with the TiO_2 .

In pure mesoporous TiO_2 , the anatase particles aggregate near the end of the rutile nanorods (Figure 1).¹⁶ 2D exchange ^{129}Xe NMR data have shown that Xe exchanges rapidly between these

two environments. The cross peaks in 2D exchange (EXSY) NMR spectra show that exchange takes place between both types of pores and the free gas with a short mixing time of 5 ms, indicating that these two types of pores are well connected. Although the pores are relatively well connected in pure mesoporous TiO_2 , the observation of two distinct resonances indicates that the exchange rate between the pores in anatase and rutile must be slower than the difference in chemical shift frequencies between anatase and rutile pores. The disappearance of two resonance peaks is most likely due to further increased interconnectivity between the anatase and rutile TiO_2 pores for hybrid TiO_2 –FGSs as compared to those for pure mesoporous TiO_2 . If the exchange of Xe between anatase and rutile pores is faster than the chemical shift difference between these two types of pores, the ^{129}Xe NMR spectrum would give one resonance peak averaged over the signals from both pores. As shown in Figure 3, the resonance frequency observed in a coalescence peak for TiO_2 –FSG is between the two resonance lines observed for pure mesoporous TiO_2 . Hence, a faster exchange of Xe between pores formed by anatase particles and the mesopore channels comprised of rutile nanorods after insertion of functionalized graphene sheets results in a single resonance peak for the hybrid TiO_2 –FGSs.

Variable-temperature continuous flow HP ^{129}Xe spectra for pure mesoporous TiO_2 are presented in Figure 4 where the top spectrum was recorded at 183 K; the temperature was raised in 20 K increments to 363 K. Because of the increased adsorption at lower temperature, a larger signal for Xe adsorbed on the pore surfaces was observed as compared to the signal associated with the void space. The slower exchange between the gas phase and adsorbed Xe at reduced temperature results in higher observed chemical shifts. Figure 4 shows two resonance peaks for adsorbed xenon at temperatures from 263 to 363 K. As the temperature decreases, the chemical shifts for both resonances increase, but at different rates. The signals collapse into one peak at temperatures below 263 K. The temperature-dependent ^{129}Xe NMR data confirm the coexistence of two distinct peaks at temperatures above 243 K, indicating that there are at least two different pore environments in mesoporous TiO_2 in which Xe can adsorb.

For comparison, variable-temperature CF HP ^{129}Xe NMR measurements were also taken for hybrid TiO_2 samples in Figure 5. Unlike the two peaks observed for pure mesoporous TiO_2 (Figure 3), a single large peak at lower chemical shift is observed for hybrid TiO_2 –graphene (Figure 4) at temperatures above 283 K. Upon decreasing the temperature, a small peak appears at a lower chemical shift as compared to the main large peak starting at temperatures below 283 K. In contrast to the large peak associated with the pores of rutile TiO_2 , the chemical shift of this small resonance does not change with the temperature, and the peak becomes broader as the temperature is decreased. This signal is not observable at temperatures below 223 K, which may be because the signal is too broad to be discerned at low temperatures. The temperature behavior for this small peak is rather unusual when compared to those for the peaks that are associated with the pores in nano- or mesoporous silica or high surface area TiO_2 . On the basis of this unique temperature behavior, the small peak cannot be associated with any pores present in the TiO_2 nanostructure alone. We assigned a weak, broad signal around ca. 50–60 ppm at 243–283 K (Figure 5) to xenon interacting with graphene. Because there is no such peak observed in pure mesoporous TiO_2 (Figure 4) and both pure mesoporous TiO_2 and hybrid TiO_2 –graphene

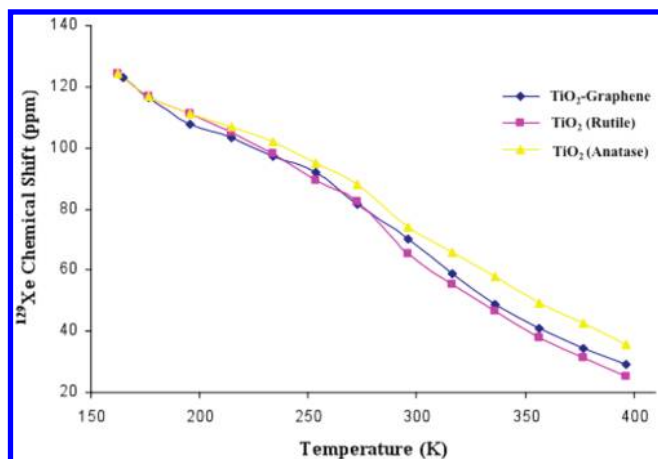


Figure 6. CF HP ^{129}Xe chemical shift for adsorbed xenon as a function of temperature for rutile and anatase pores in mesoporous TiO_2 and pores in self-assembled TiO_2 –FGS hybrids. The dashed lines are a visual guide only.

contain the same amount of rutile and anatase phases, this lower chemical shift peak is most likely caused by the addition of graphene sheets. It is possible that xenon adsorbed between closely spaced graphene sheets could produce a weak resonance peak observed at lower chemical shift because Xe has a stronger interaction with TiO_2 surfaces than with the graphene sheets. Therefore, at higher temperature, Xe is thought to adsorb primarily on the TiO_2 surface, and no resonance is to be expected for Xe interacting with graphene sheets. However, at lower temperature, the adsorbed Xe concentration increases. We then begin to observe the signal from xenon adsorbed within the interlayer spaces of the layered graphene sheets. Because graphene has a large two-dimensional surface, Xe exhibits a different exchange mechanism within the graphene interlayer space as compared to those nano- or mesopores of TiO_2 . This results in a unique temperature-dependent behavior.

The temperature dependence of ^{129}Xe chemical shift upon adsorption to mesoporous TiO_2 and hybrid TiO_2 –graphene hybrid materials is shown in Figure 6 where TiO_2 (rutile) and TiO_2 (anatase) represent the pores in mesoporous TiO_2 that give rise to the ^{129}Xe NMR resonance peaks at lower and higher chemical shifts shown in Figure 3, respectively. Figure 6 shows similar temperature-dependent ^{129}Xe chemical shifts for mesoporous TiO_2 (rutile) and TiO_2 –FGSs, whereas the chemical shift for xenon adsorbed between mesopores of rutile and anatase in mesoporous TiO_2 is notably different. It is understandable that we observed similar temperature-dependent chemical shift curves for both hybrid TiO_2 –graphene and TiO_2 (rutile) because the hybrid TiO_2 –FGSs are comprised principally of rutile TiO_2 . The contrasting temperature-dependent behavior for TiO_2 (rutile) and TiO_2 (anatase) can be attributed to the difference in geometric structures between the crystalline anatase and rutile phases.²⁵

Temperature-dependent chemical shift data can be used to determine physical parameters related to the adsorption properties of materials. Variations in the ^{129}Xe chemical shift with temperature can be fit to a parametrized model describing xenon absorption that is based upon a Henry's law isotherm, as described previously.⁴¹ In the fast exchange approximation with weak adsorption, the temperature dependence of the observed

Table 1. Heat of Adsorption (ΔH) and Characteristic Chemical Shift (δ_s) for Xenon Adsorbed in the Different TiO_2 Samples, Along with the Estimated Pore Diameters Based upon Spherical (D_s) and Cylindrical (D_c) Models

samples	ΔH (kJ/mol)	δ_s (ppm)	D_s (nm)	D_c (nm)
graphene	NA	NA	NA	NA
TiO_2 –graphene	15.1	114	5.3	3.2
TiO_2 (rutile)	16.0	116	5.7	3.8 ^a
TiO_2 (anatase)	12.9	122	3.8 ^a	2.6

^a Pore diameters are determined from models discussed in this Article.

chemical shifts, δ_{obs} , for arbitrary pore sizes can be expressed as:

$$\delta_{\text{obs}} = \delta_s \left(1 + \frac{B}{T e^{-\Delta H_{\text{ads}}/RT}} \right); B = \left(\frac{V_g}{S} \right) K_0^{-1} \quad (1)$$

where V_g is the free volume inside TiO_2 , T is the temperature, S is a specific surface area, K_0 is the pre-exponential term of Henry's constant, R is the universal gas constant, ΔH_{ads} is the heat of adsorption, and δ_s is the component of the observed ^{129}Xe chemical shift characteristic of the interaction between xenon and the surface.

Table 1 lists the ΔH_{ads} and δ_s values obtained from fits of these variable-temperature chemical shift curves. The δ_s values range from 114 to 122 ppm for mesoporous TiO_2 and hybrid TiO_2 –FGSs samples, which are comparable to the 109 ppm previously reported for nonporous anatase TiO_2 obtained using thermally polarized Xe in a sealed high pressure cell.³³ It is not surprising to observe similar characteristic chemical shifts because δ_s correlates with the surface chemical composition, and Ti–O chemical bonding predominates in these samples. However, the small variance in δ_s for all samples is due to other subtle differences such as the level of hydration, reduced oxidation state, or the presence of different TiO_2 phases. The observed ΔH_{ads} values for these samples are in the range from 12 to 16 kJ/mol, which is consistent with what is generally seen for physical adsorption of Xe on solid surfaces; this has been observed before in numerous micro- and mesoporous materials.^{41,42} Table 1 also shows a larger heat of adsorption of 16.0 kJ/mol for TiO_2 (rutile) than that of 12.9 kJ/mol for TiO_2 (anatase). In agreement with the observation of different slopes in temperature-dependent chemical shift data for Xe adsorbed on TiO_2 (rutile) and TiO_2 (anatase), the difference in ΔH_{ads} values suggests the existence of two types of binding sites for Xe adsorbed on TiO_2 (rutile) and TiO_2 (anatase) pore surfaces. Because both rutile and anatase pores are comprised of TiO_2 , the binding sites are largely determined by the geometries of the pore surfaces. The different geometries of pore surfaces may arise from the coexistence of different crystalline phases such as anatase and rutile TiO_2 . Hence, TiO_2 (rutile) and TiO_2 (anatase) are associated with the anatase and rutile phases, in agreement with the XRD and TEM data.¹⁶ Pore diameters for both mesoporous TiO_2 and hybrid TiO_2 –FGSs samples were estimated using empirical chemical shift–pore size correlations developed for inorganic systems like MCMs and zeolites.^{43,44} Table 1 displays the pore sizes derived from the ^{129}Xe NMR data in the context of both spherical and cylindrical pore models for all TiO_2 samples. For a given model, the resonance with a larger chemical shift often corresponds to a smaller pore size. Because the interparticle spacing is representative of more spherical pores than cylindrical pores, it is reasonable to use the spherical pore model to estimate the pore sizes for

all pores formed from the aggregation of the nanoparticles. However, the cylindrical pore model is best suited for the cylindrical mesoporous channels observed in rutile TiO_2 by TEM. Using appropriate models, both rutile and anatase pores in mesoporous TiO_2 have similar sizes as shown in Table 1. The results derived in the context of spherical and cylindrical models reported in Table 1 are to be treated as approximations. The pore sizes should be regarded with caution, as there may be an unaccounted scaling factor due to differences in the chemical composition. However, we believe that the result on the comparison of two types of pores is sufficiently reliable. The pore size for rutile TiO_2 in hybrid TiO_2 –FGSs is also similar to that for pure mesoporous TiO_2 . Even though the chemical shift for TiO_2 (anatase) is larger than that for TiO_2 (rutile), we obtained similar pore sizes because of the difference in pore geometries. The pore diameter of 3–4 nm for meso- TiO_2 determined from the ^{129}Xe NMR data is in agreement with the TEM and BET results.¹⁶ Unlike BET, ^{129}Xe NMR allows us to identify pores of similar size in different phases of TiO_2 .

Our comparative HP ^{129}Xe NMR results from this study have shown that ^{129}Xe NMR is a powerful technique for probing any changes in porosity and interconnectivity of the pores caused by the addition of a small amount of functionalized graphene sheet (1 wt %) into the network of mesoporous TiO_2 . The information on the interconnectivity of the pores is critical for understanding transport properties in porous materials. Such information is difficult to obtain using conventional techniques such as BET, XRD, or TEM. Because spin-polarized Xe gas percolates through the interconnected pores and samples the local pore environments, HP ^{129}Xe NMR has the unique advantage of directly probing not only these buried interfaces but also the interconnectivity between the pores. On the basis of the comparative HP ^{129}Xe NMR studies of pure mesoporous TiO_2 before and after the insertion of FGSs, the changes in HP ^{129}Xe NMR spectra upon addition of the functionalized graphene sheets (FGSs) indicate that TiO_2 and graphene are mixed uniformly on the nanoscale, and the resulting hybrid nanostructure has higher channel connectivity among different domains. This higher connectivity accompanied by well-separated graphene sheets in the TiO_2 nanostructural network may be one of major contributing factors that promotes enhanced lithium insertion/extraction in the hybrid material.

CONCLUSIONS

Our ^{129}Xe NMR study has shown that Xe is sensitive to any change in TiO_2 nanostructure upon insertion of a small amount of graphene into the mesoporous network. A relatively narrow ^{129}Xe single peak is observed for the self-assembled hybrid TiO_2 –FGSs. In contrast, however, there are two resonance peaks corresponding to rutile TiO_2 and anatase TiO_2 in pure mesoporous TiO_2 . The HP ^{129}Xe NMR results from our comparative study suggest that TiO_2 and graphene are mixed uniformly on the nanoscale, and the resulting hybrid nanostructure has better channel connectivity among the resident domains, thereby enhancing Li transport throughout the structure.

AUTHOR INFORMATION

Corresponding Author

*E-mail: li_qiong_wang@brown.edu.

ACKNOWLEDGMENT

The HP ^{129}Xe NMR work was supported by the Materials Sciences and Engineering Division, Office of Basic Energy Sciences, U.S. Department of Energy (US DOE). The synthesis effort was conducted under the Laboratory Directed Research and Development Program (LDRD) at Pacific Northwest National Laboratory (PNNL). PNNL is a multiprogram national laboratory operated for the USDOE by Battelle Memorial Institute under Contract DE-AC06-76RL0 1830.

REFERENCES

- (1) Moudrakovski, I. L.; Tersikh, V. V.; Ratcliffe, C. I.; Ripmeester, J. A.; Wang, L.-Q.; Shin, Y.; Exarhos, G. J. *J. Phys. Chem. B* **2002**, *106*, 5938.
- (2) Ripmeester, J. A. *J. Am. Chem. Soc.* **1982**, *104*, 289.
- (3) Ito, T.; Fraissard, J. *J. Chem. Phys.* **1982**, *76*, 5225.
- (4) Ratcliffe, C. I. *Annu. Rep. NMR Spectrosc.* **1998**, *36*, 124.
- (5) Raftery, D.; Chmelka, B. F. *NMR*. **1994**, *30*, 111.
- (6) (a) Grover, B. C. *Phys. Rev. Lett.* **1978**, *40*, 391. (b) Happer, W.; Miron, E.; Schaefer, S.; Schreiber, D.; van Wingen, W. A.; Zeng, X. *Phys. Rev. A* **1984**, *29*, 3092. (c) Driehuis, B.; Cates, G. D.; Miron, E.; Sauer, K.; Walter, D. K.; Happer, W. *Appl. Phys. Lett.* **1996**, *69*, 1668.
- (7) Hu, Y. S.; Kienle, L.; Guo, Y. G.; Maier, J. *Adv. Mater.* **2006**, *18*, 1421–1426.
- (8) Moskon, J.; Dominko, R.; Gaberscek, M.; Cerc-Korosec, R.; Jamnik, J. *J. Electrochem. Soc.* **2006**, *153*, A1805–A1811.
- (9) Baudrin, E.; Cassignon, S.; Koesch, M.; Jolivet, J. P.; Dupont, L.; Tarascon, J. M. *Electrochem. Commun.* **2007**, *9*, 337–342.
- (10) Zukalova, M.; Kalbac, M.; Kavan, L.; Exnar, I.; Gratzel, M. *Chem. Mater.* **2005**, *17*, 1248–1255.
- (11) Zhou, Y. K.; Cao, L.; Zhang, F. B.; He, B. L.; Li, H. L. *J. Electrochem. Soc.* **2003**, *150*, A1246–A1249.
- (12) Reddy, M. A.; Kishore, M. S.; Pralong, V.; Caignaert, V.; Varadaraju, U. V.; Raveau, B. *Electrochem. Commun.* **2006**, *8*, 1299–1303.
- (13) Jiang, C. H.; Honma, I.; Kudo, T.; Zhou, H. S. *Electrochem. Solid-State Lett.* **2007**, *10*, A127–A129.
- (14) Armstrong, G.; Armstrong, A. R.; Bruce, P. G.; Reale, P.; Scrosati, B. *Adv. Mater.* **2006**, *18*, 2597–2600.
- (15) Armstrong, A. R.; Armstrong, G.; Canales, J.; Bruce, P. G. *Angew. Chem., Int. Ed.* **2004**, *43*, 2286–2288.
- (16) Wang, D. H.; Choi, D. W.; Yang, Z. G.; Viswanathan, V. V.; Nie, Z. M.; Wang, C. M.; Song, Y. J.; Zhang, J. G.; Liu, J. *Chem. Mater.* **2008**, *20*, 3435.
- (17) Antonelli, D. M.; Ying, J. Y. *Angew. Chem.* **1995**, *107*, 2202–2205. Antonelli, D. M.; Ying, J. Y. *Angew. Chem., Int. Ed.* **1995**, *34*, 2014–2017.
- (18) Yang, P.; Zhao, D.; Margolese, D. I.; Chmelka, B. F.; Stucky, G. D. *Nature* **1998**, *396*, 152–155.
- (19) Elder, S. H.; Gao, Y.; Li, X.; Liu, J.; McCready, D. E.; Windisch, C. F. *Chem. Mater.* **1998**, *10*, 3140–3145.
- (20) Li, D. L.; Zhou, H. S.; Honma, I. *Nat. Mater.* **2004**, *3*, 65–72.
- (21) Shibata, H.; Ogura, T.; Mukai, T.; Ohkubo, T.; Sakai, H.; Abe, M. *J. Am. Chem. Soc.* **2005**, *127*, 16396–16397.
- (22) Crepaldi, E. L.; Soler-Illia, G.; Grosso, D.; Cagnol, F.; Ribot, F.; Sanchez, C. *J. Am. Chem. Soc.* **2003**, *125*, 9770–9786.
- (23) Stone, V. F.; Davis, R. J. *Chem. Mater.* **1998**, *10*, 1468–1474.
- (24) Zhou, Y.; Antonietti, M. *J. Am. Chem. Soc.* **2003**, *125*, 14960–14961.
- (25) Wang, L.-Q.; Wang, D.; Liu, L.; Exarhos, G. J.; Pawsey, S.; Moudrakovski, I. *J. Phys. Chem. C* **2009**, *113*, 6577.
- (26) Wang, D.; Daiwon Choi, D.; Li, J.; Yang, Z.; Nie, Z.; Kou, R.; Hu, D.; Wang, C.; Saraf, L. V.; Zhang, J.; Aksay, I. A.; Liu, J. *ACS Nano* **2009**, *3*, 907.
- (27) Berger, C.; Song, Z. M.; Li, X. B.; Wu, X. S.; Brown, N.; Naud, C.; Mayo, D.; Li, T. B.; Hass, J.; Marchenkov, A. N.; Conrad, E. H.; First, P. N.; de Heer, W. A. *Science* **2006**, *312*, 1191–1196.

- (28) Novoselov, K. S.; Geim, A. K.; Morozov, S. V.; Jiang, D.; Zhang, Y.; Dubonos, S. V.; Grigorieva, I. V.; Firsov, A. A. *Science* **2004**, *306*, 666–669.
- (29) Stankovich, S.; Dikin, D. A.; Dommett, G. H. B.; Kohlhaas, K. M.; Zimney, E. J.; Stach, E. A.; Piner, R. D.; Nguyen, S. T.; Ruoff, R. S. *Nature* **2006**, *442*, 282–286.
- (30) Ramanathan, T.; Abdala, A. A.; Stankovich, S.; Dikin, D. A.; Herrera-Alonso, M.; Piner, R. D.; Adamson, D. H.; Schniepp, H. C.; Chen, X.; Ruoff, R. S.; Nguyen, S. T.; Aksay, I. A.; Prud'homme, R. K.; Brinson, L. C. *Nat. Nanotechnol.* **2008**, *3*, 327–331.
- (31) McAllister, M. J.; LiO, J. L.; Adamson, D. H.; Schniepp, H. C.; Abdala, A. A.; Liu, J.; Herrera-Alonso, M.; Milius, D. L.; CarO, R.; Prud'homme, R. K.; Aksay, I. *Chem. Mater.* **2007**, *19*, 4396–4404.
- (32) Schniepp, H. C.; Li, J. L.; McAllister, M. J.; Sai, H.; Herrera-Alonso, M.; Adamson, D. H.; Prud'homme, R. K.; Car, R.; Saville, D. A.; Aksay, I. A. *J. Phys. Chem. B* **2006**, *110*, 8535–8539.
- (33) Gomez-Navarro, C.; Weitz, R. T.; Bittner, A. M.; Scolari, M.; Mews, A.; Burghard, M.; Kern, K. *Nano Lett.* **2007**, *7*, 3499–3503.
- (34) Si, Y.; Samulski, E. T. *Nano Lett.* **2008**, *8*, 1679–1682.
- (35) Wang, D. H.; Ma, Z.; Dai, S.; Liu, J.; Nie, Z. M.; Engelhard, M. H.; Huo, Q. S.; Wang, C. M.; Kou, R. *J. Phys. Chem. C* **2008**, *112*, 13499–13509.
- (36) Stankovich, S.; Dikin, D. A.; Piner, R. D.; Kohlhaas, K. A.; Kleinhammes, A.; Jia, Y.; Wu, Y.; Nguyen, S. T.; Ruoff, R. S. *Carbon* **2007**, *45*, 1558.
- (37) Ruset, I. C.; Ketel, S.; Hersman, F. W. *Phys. Rev. Lett.* **2006**, *96*, 053002.
- (38) Bielecki, A.; Burum, D. J. *Magn. Reson.* **1995**, *116*, 215.
- (39) McAllister, M. J.; LiO, J. L.; Adamson, D. H.; Schniepp, H. C.; Abdala, A. A.; Liu, J.; Herrera-Alonso, M.; Milius, D. L.; Caro, R.; Prud'homme, R. K.; Aksay, I. A. *Chem. Mater.* **2007**, *19*, 4396–4404.
- (40) Schniepp, H. C.; Li, J. L.; McAllister, M. J.; Sai, H.; Herrera-Alonso, M.; Adamson, D. H.; Prud'homme, R. K.; Car, R.; Saville, D. A.; Aksay, I. *J. Phys. Chem. B* **2006**, *110*, 8535–8539.
- (41) Tersikh, V.; Moudrakovski, I.; Mastikhin, V. *J. Chem. Soc., Faraday Trans.* **1993**, *89*, 4239.
- (42) Tersikh, V. V.; Moudrakovski, I. L.; Breeze, S. R.; Lang, S.; Ratcliffe, C. I.; Ripmeester, J. A.; Sayari, A. *Langmuir* **2002**, *18*, 5653.
- (43) Tersikh, V. V.; Moudrakovski, I. L.; Breeze, S. R.; Lang, S.; Ratcliffe, C. I.; Ripmeester, J. A.; Sayari, A. *Langmuir* **2002**, *18*, 5653.
- (44) Ripmeester, J. A.; Ratcliffe, C. I. *J. Phys. Chem.* **1990**, *94*, 7652.